High Frequency Tomography Using Bottom-Mounted Transducers

James K. Lewis, Peter J. Stein, Subramaniam Rajan, Jason Rudzinsky*,
Amy Vandiver, The KauaiEx Group

Scientific Solutions, Inc., P.O. Box 1029, Kalaheo, HI 96741
*Applied Physical Sciences, Corp., 2 State Street, Suite 300, New London, CT 06320

Abstract. The sources and receivers at the Pacific Missile Range Facility (PMRF) provide for performing acoustic tomography. A primary problem is that acoustic signals of interest interact with the ocean surface, and surface wave fields result in considerable variability in arrival times. Arrival times of rays that have interacted with the moving ocean surface are obtained by averaging over a number of pings to eliminate errors due to Doppler shifts. We also present transforms using differences between observed travel time anomalies and those calculated using an ocean circulation model to make adjustments to model-predicted water temperatures, salinities, and currents (model-oriented acoustic tomography).

INTRODUCTION

The Pacific Missile Range Facility (PMRF) off Kauai, Hawaii, has 15 bottom-mounted sources (8-15 kHz) and 178 bottom-mounted receivers. These assets provide for the possibility of performing acoustic tomography throughout the range. The distances between source-receiver pairs in the shallow water range are relatively small (≤10 km), meaning arrival times are readily detectable. However, the acoustic signals of most interest interact with the ocean surface. As a result, the surface wave field results in considerable variability in arrival times at 8-15 kHz.

Arrival time anomalies are determined relative to a monthly sound velocity structure based on a three-dimensional grid of a hydrodynamic model of the PMRF region. The model provides its own estimate of the four-dimensional sound speed structure. We present transforms for determining a model-related travel time anomaly along the path of a transmitted acoustic ray. The differences between the two travel time anomalies can be transformed back to adjustments of model-predicted water temperatures, salinities, and currents using the Physical-space Statistical Analysis System (PSAS) data assimilation scheme[1].

THE OCEAN MODELS FOR PMRF

An adaptation of the hydrodynamic model of the Blumberg and Mellor[2] has been implemented for Kauai, Hawaii (Fig. 1). Bathymetry is from the Smith-Sandwell topography[3] augmented with data from NOAA and PMRF.
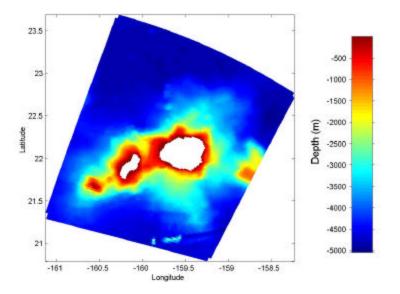
FIGURE 1. Domain and depth field for the Kauai ocean model.

Observed temperature and salinity (T-S) characteristics were used in specifying the vertical resolution of the model. The vertical grid structure has 28 active levels with higher resolution within the top 100 m and at depths at which salinity extremes exist.

We utilized the open boundary condition presented in Lewis et al.[4], specifying the M_2, S_2, N_2, O_1, K_1, and P_1 tidal sea level elevations and phases along the open boundaries of the model domains. The boundary values were from the TPXO.3[5] tidal model but "tuned" to match observed amplitudes and phases for Kauai.

Surface waves were modeled using Delft University of Technology's SWAN (Simulating WAves Nearshore[6]). SWAN is a two-dimensional wave spectra model that can use a curvilinear-orthogonal grid. This allows SWAN to use the same computational grid (and associated depths) as the ocean circulation model.

Initialization and Forcing Fields

The model uses the Navy's daily Modular Ocean Data Assimilation System (MODAS) to estimate the three-dimensional T-S structure. This is used to introduce the mesoscale circulation field into the model. Atmospheric forcing from the National Centers for Environmental Prediction (NCEP) includes momentum, heat, and mass fluxes at the air-sea interface. The SWAN model is forced by the NCEP surface wind velocity and, wave spectra along the open boundaries from NOAA's WaveWatch III wave model is used to account for wave energy that propagates into the region.

Since waves can have a significant impact on ocean circulation[7], the circulation model utilized the surface wave model results to calculate 1) wave-enhanced bottom friction, 2) Stokes drift and the Coriolis wave stress, 3) radiation stresses, 4) wave-related mixing length at the ocean surface, and 5) the virtual tangential surface stress.

CONSTRUCTS RELATED TO THE PSAS DATA ASSIMILATION

Simulating Acoustic Paths and Travel Times

We used the locations of the PMRF sources and receivers, model-predicted sound speed profiles (SSP), and acoustic propagation models to calculate paths of acoustic rays between the sources and receivers. In many cases, direct-path rays and single-surface bounce rays had arrival times very close to one another. This was verified with actual field data.

Our simulations indicated that multiple surface bounce acoustic rays were stable in the paths they took from source to receiver, and their arrival times were well separated from the earlier arrivals. Moreover, multiple surface bounce rays provide a better sampling of the water column. Due to the drop in signal-to-noise for higher multiple surface bounce acoustic paths, we concentrated on analyzing paths that bounced off the ocean surface only twice. Our analyses require a reference sound speed structure c_R. This was determined using monthly climatological T-S fields for the region. The PSAS assimilation scheme also requires reference fields for T, S, and current velocities. Again, the monthly climatological T-S fields were used, while a reference velocity of 0 m/s was used throughout space and time.

Observed and Model-Predicted Travel Time Anomalies

The observed travel time t_o for an acoustic path is combined with a reference ocean arrival time t_R to determine a travel time anomaly: $\Delta\tau_R = t_o - t_R$. Knowing the path an acoustic ray would take through the model domain (individual grid cells denoted by i = 1,2,3,…,N), we can calculate an estimated arrival time: $t = \Sigma [\Delta L_i / (c_i + U_i)]$, where c_i is the sound speed in the ith grid cell, ΔL_i is the distance that the ray travels through the ith grid cell, and U_i is the component of the three-dimensional current along a particular direction of interest responsible for effectively increasing or decreasing the sound speed.

The reference travel time t_R uses the reference T-S vs. depth to give individual values for $c_{R,i}$, and $U_{R,i}$ is always zero:

$$t_R = \Sigma [\Delta L_i / c_{R,i}]. \tag{1}$$

We used a different expression when dealing with the model-predicted travel time anomalies. A model-predicted travel time is

$$t_m = \Sigma [\Delta L_i / (c_{m,i} + U_{m,i})] \tag{2}$$

where the m denotes model-predicted values. The model sound speed anomaly is

$$\Delta c_i = (c_{m,i} + U_{m,i}) - c_{R,i}. \tag{3}$$

Rearranging (3), substituting into (2), linearizing using $c_{Ri}^2 >> \Delta c_i^2$, and rearranging the result in terms of a travel time anomaly give

$$\Delta t_m(t) = -\sum_{i=1}^{N} \frac{\Delta L_i \Delta c_i(t)}{c_{R,i}^2} + e_{LIN}(t) + e_{DIS}(t) = \mathbf{b} \, ? \, \mathbf{c}^T + e_{FM}(t). \tag{4}$$

where N is the number of model grid cells through which the ray travels. Errors associated with the linearization approximation are in $e_{LIN}(t)$, and the discretization errors are in $e_{DIS}(t)$. The $e_{LIN}(t)$ term also includes those errors resulting from the assumption that the ray path does not vary with time.

On the right hand side of (4), we have represented the summation as the multiplication of the **b** vector of the constant $-\Delta L_i/c^2_{R,i}$ terms and the **Dc** vector of the time-varying terms $\Delta c_i(t)$. All errors have been combined into $e_{FM}(t)$.

We can group all of the model-related acoustic travel time anomaly measurements into a *measurement matrix equation*:

$$\mathbf{z}(t) = \mathbf{H}\mathbf{x}(t) + \mathbf{e}_{\mathbf{FM}}(t) + \mathbf{e}_z(t). \tag{5}$$

The *M* travel time anomaly measurements ($\Delta\tau$'s) of P source-receiver transects made at a given time *t* are in the column vector $\mathbf{z}(t)$. The rows of the **H** matrix are the **b** vectors. The number of columns in **H** will be the maximum of the N's (N_{max}), and there can be a number of zero entries in **H**. The **Dc** for each grid cell through which a ray path travels is the N_{max} column vector **x**.

Tomographic Transformation of Equation (5)

Equation (5) must be transformed to relate travel time anomalies to ocean model variables. We express the sound speed as a reference c_R and a perturbation:

$$c = c_R + \frac{\partial c}{\partial T}\Delta T + \frac{\partial c}{\partial S}\Delta S + U = c_R + \mathbf{d}c. \tag{6}$$

For small T and S variations, we can approximate the two partial derivatives as:

$$\frac{\partial c}{\partial T}\Delta T \approx 4.947\,\Delta T = \mathbf{a}\,\Delta T \qquad \frac{\partial c}{\partial S}\Delta S \approx 1.34\,\Delta S = \mathbf{b}\,\Delta S$$

where α has units of m/s/°C and β has units of m/s/ppt. We can rearrange (6) to give

$$\mathbf{D}c_i = \alpha\Delta T + \beta\Delta S + U \tag{7}$$

We use (7) to transform (5) or, in its form in (4), the expression for the model-related travel time anomaly along a given path of N grid cells:

$$\mathbf{D}t_m = \mathbf{b}\,\mathbf{D}v^T \tag{8}$$

where now

$$\mathbf{b} = [-\Delta L_1/(\Delta c_{R,1})^2 \quad -\Delta L_1\alpha\,/(\Delta c_{R,1})^2 \quad -\Delta L_1\beta\,/(\Delta c_{R,1})^2 \quad \ldots$$
$$-\Delta L_N\,/(\Delta c_{R,N})^2 \quad -\Delta L_N\alpha\,/(\Delta c_{R,N})^2 \quad -\Delta L_N\beta\,/(\Delta c_{R,N})^2]$$

and the $\boldsymbol{D}v$ vector is

$$\boldsymbol{D}v = [U_1 \quad \Delta T_1 \quad \Delta S_1 \quad \ldots \quad U_N \quad \Delta T_N \quad \Delta S_N].$$

Each of the parameters in $\boldsymbol{D}v$ is the known model-predicted variable relative to the reference value. We will use the above b for the rows in $\mathbf{H}$ and $\boldsymbol{D}v$ for the column vector $\mathbf{x}$. Our tomographic relationship is (8), relating acoustics to T, S, and U.

Assimilation of Tomographic Information Into The Ocean Model

We define ocean parameters as $\mathbf{x}$, $\mathbf{x^F}$ and $\mathbf{x^A}$, vectors representing the *true state*, the *forecasted estimate*, and the *analysis estimate*, respectively. The vectors $\mathbf{x}$, $\mathbf{x^F}$ and $\mathbf{x^A}$ are time dependent, and the three-dimensional T, S, and U fields form our state vector.

The basic expression to determine the analysis (updated) field combines the forecast estimate $\mathbf{x^F}$ with the acoustic-related measurements $\mathbf{z}_R$ (the $\Delta\tau_R$'s) using the model-related measurement matrix $\mathbf{H}$ as follows (the PSAS formulation)[1]:

$$\mathbf{x^A} = \mathbf{x^F} + \mathbf{K}\big(\mathbf{z}_R - \mathbf{Hx^F}\big). \tag{9}$$

Here, $\mathbf{z}_R$ **-** $\mathbf{Hx^F}$ is the *measurement residual.* $\mathbf{K}$ is the residual (Kalman) gain matrix:

$$\mathbf{K} = \mathbf{P_F}\mathbf{H}^T(\mathbf{HP_F}\mathbf{H}^T + \mathbf{R})^{-1}.$$

$\mathbf{P_F}$ is the forecast error covariance

$$\mathbf{P_F} = E\Big[\big(\mathbf{x}-\mathbf{x^F}\big)\big(\mathbf{x}-\mathbf{x^F}\big)^T\Big]$$

and $\mathbf{R}$ is the observation error covariance

$$\mathbf{R} = E\Big[(\mathbf{e_{FM}} + \mathbf{e_z})\,(\mathbf{e_{FM}} + \mathbf{e_z})^T\Big] = \mathbf{R_{FM}} + \mathbf{R_z}.$$

Here, the total observation error covariance is expressed as a sum of the model error covariance and the measurement error covariance. The former can be estimated using archived ocean model output to evaluate the expected travel time differences between a linear discrete acoustic model (such as that embodied here in the measurement matrix $\mathbf{H}$) and an acoustic propagation model based on a solution to the wave equation. The latter term can be estimated from the second order statistics of an ensemble of arrival time observations. The Kalman gain distributes the measurement residual throughout the forecast model domain. Corrections are assigned mostly to

regions closest to the observations and where the forecast model uncertainty is highest.

Use of Equation (9) For This Study

For this study, (9) was simplified assuming that travel time anomalies were primarily a result of the differences between predicted and ocean water temperatures. In this case, $\mathbf{x^F}$ and $\mathbf{x^A}$ are vectors of forecasted and analysis temperatures relative to monthly reference temperatures: $\mathbf{x^F} = \mathbf{T_{model}} - \mathbf{T_{reference}}$ and $\mathbf{x^A} = \mathbf{T_{analysis}} - \mathbf{T_{reference}}$. Since $\mathbf{T_{reference}}$ appears on both sides of (9), that the expression can be simplified to

$$\mathbf{T_{analysis}} = \mathbf{T_{model}} + \mathbf{K}\left(\mathbf{z}_R - \mathbf{Hx^F}\right).$$

The rows of the $\mathbf{H}$ matrix now consist of

$$\mathbf{b} = [-\Delta L_1 \alpha /(\Delta c_{R,1})^2 \ \ -\Delta L_2 \alpha /(\Delta c_{R,1})^2 \ \ \ldots \ \ -\Delta L_N \alpha /(\Delta c_{R,N})^2]$$

for each ray path. $\mathbf{z}_R$ is the column vector of "observed" travel time anomalies. Thus, all the terms on the RHS of (9) are defined, and we can solve for $\mathbf{T_{analysis}}$.

Calculating Covariance Functions

In this study, the error covariance matrices $\mathbf{P_F}$ and $\mathbf{R}$ were derived from the estimates of the spatial covariance of the model-predicted temperatures:

$$P_F = E\left[\left(T_{MODEL} - E(T_{MODEL})\right)\left(T_{MODEL} - E(T_{MODEL})\right)^T.\right] \tag{10}$$

$\mathbf{P_F}$ can be estimated using ensembles of model temperature time series. This always results in over-estimating the error covariance. As a result, the rate of spatial decorrelation of a model variable is underestimated. Thus we would expect the observations to be more spatially limited in their impact on the analysis fields.

Implementation

In implementing our data assimilation scheme, we limited the model grid cells impacted by acoustic observations to those within 10 km of any ray path being considered. If L_{max} is the number of grid cells within the 10 km range, then $\mathbf{P_F H^T}$ for the p ray is an L_{max} column vector. There are 12 monthly column vectors for any ray path. All terms in the $\mathbf{HP^F H^T}$ matrix are known, and each monthly matrix was calculated. $\mathbf{HP^F H^T}$ was used to represent the $\mathbf{R}$ array until some future time when we can make an accurate estimate of $\mathbf{R}$. The monthly $\mathbf{HP^F H^T}$ matrices were inverted and multiplied by $\mathbf{P_F H^T}$ to give 12 L_{max} x P_{max} arrays, where P_{max} is the number of ray paths being considered.

Thus, the analysis and assimilation software only requires the monthly databases of 1) the $\mathbf{P_F H^T (HP^F H^T)^{-1}}$ elements, 2) the reference temperatures along the acoustic paths being considered (for $\mathbf{Dv}$ in (8)), and 3) the $-\alpha \ \Delta L_N / c_{R,N}^2$ values (for $\mathbf{b}$ in (8)).

ACOUSTIC DATA ACQUISITION SYSTEM (ADAS)

To allow near autonomous repetitive collection of acoustic data using the PMRF hydrophone network, we implemented an Acoustic Data Acquisition System (ADAS). Transmissions can be made from any the PMRF acoustic projectors. Any combination of the PMRF receivers can be specified for recording acoustic signals.

Each transmitted signal is replica-correlated with the received signal. The received signal is modeled as a sum of ray arrivals given by

$$r(t) = \sum_n a_n s(t - \boldsymbol{t}_n)$$

where a_n is the weight associated with each arrival, s(t) is the transmitted signal and τ_n is the delay associated with each arrival. This model is not strictly correct when dealing with propagation in a shallow water environment. However, at source frequencies of 10 kHz, the effect of dispersion is negligible, and the errors in the model can be ignored.

Two choices for the transmit signal were a chirp signal and a phase-coded sequence. In areas where the acoustic signal interacts with waves on the ocean surface, there can be a Doppler shift that compresses or elongates the signal envelop. Matched filter output of this Doppler-shifted signal gives rise to errors in a) estimating the arrival time and b) the amplitude of the matched filter output of each arrival. Analysis of errors in estimating arrival times showed that the errors in the phase-coded sequence were less than that of the chirp signal. However, the amplitude of the matched filter output remained practically unaltered in the case of chirp signal, while in the phase-coded sequence it is reduced substantially. Since averaging can eliminate the error in the arrival time due to surface motion, a chirp signal was considered a better choice for the transmit signal. The chirp signals had a center frequency of 9.5 kHz and a bandwidth of 3 kHz.

In order to improve the signal-to-noise ratio and to reduce the impact of surface motion, we averaged over a number of acoustic transmissions. Under normal circumstances, it would have been appropriate to send a large train of acoustic pulses and perform an average over this train of pulses. However, this was not possible because of "cross talk" between the transmitter and receivers. Instead, we transmitted a sequence of 12 acoustic transmissions that consisted of 4 groups separated by 8 sec. Each acoustic transmission had a duration of 0.1 sec, with an interval of 0.4 sec between each transmission. The number of pulses in a group was restricted to 3 transmissions to avoid interference due to cross talk. The distance to the nearest receiver set this limitation. The maximum distance between the source and selected receivers dictated the 8 sec separation between groups of transmissions. The string of 12 transmissions was repeated 3 times with an interval of about 30 sec.

The matched filter output for a varying number of transmissions is shown in Fig. 2. We see that a considerable enhancement of the signal-to-noise ratio is achieved by averaging over 36 transmissions. The arrival structure in Fig. 2 consists of one stronger group of arrivals followed by three weaker groups of arrivals. An eigenray[8] analysis for this particular source/receiver pair was performed using a sound
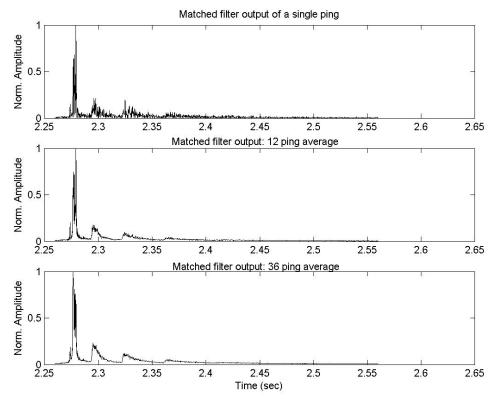
FIGURE 2. Matched filter output for a single transmission (top), an average of 12 transmissions (middle), and an average of 36 transmissions (bottom).

speed field for the region obtained from the ocean model. The earliest group of arrivals consists of rays that travel from source to receiver without interacting with either the ocean surface or bottom and others that include a ray that interacts with the surface only once and rays that hug the bottom and have repeated interactions with the bottom. The arrival time of rays that have only interactions with the bottom carry little information about the bulk of the water column. This plus the problem of delineating individual ray arrival times within the first group of arrivals lead us to neglect these arrivals in our tomography analysis.

The subsequent three arrivals in Fig. 2 correspond to rays that have 2, 3, and 4 surface bounces, respectively. We concentrated on analyzing the path that bounced off the ocean surface only twice due to the drop in signal-to-noise for higher multiple surface bounce acoustic paths (the third and fourth groups of arrivals).

The ADAS collected travel time observations for a double-surface bounce ray path just offshore of the 90 m isobath. The ray path was between a source (D9) some 3.5 km from a receiver (D12). The arrival time of a ray with two surface bounces is about 2.3 seconds. This is used to readily identify the arrival time of the two-surface bounce ray in the ADAS data. An enhanced view of the matched filter output corresponding to the arrival time for this ray (not shown) indicates a distinct peak, with other peaks that are likely the result fluctuations in arrival time caused by motion of the ocean surface and the roughness of the ocean bottom. In order to better determine an arrival time, we low-pass filtered the matched filter output.

DATA ASSIMILATION TEST CASE, JULY 2003

During June-July, 2003, a series of thermistor strings were placed along the 90 m isobath just shoreward of the D9-D12 source-receiver pair. The distance between the D9-D12 ray path and the thermistor arrays was ~0.5 km. The thermistor data provide a means of assessing the impact of assimilating the D9-D12 arrival time anomaly data into the ocean circulation model.

The ocean model was first executed without any acoustic data assimilation, and the model-predicted water temperatures were compared to the thermistor data for July 3, 2003. The rms differences between the model results and the thermistor data are shown in Fig. 3. These range from 0.4-1.5°C, with maximum differences occurring in the lower part of the water column. The bottom of the surface mixed layer is approximately 70-90 m, and tidal forcing can result in considerable semi-diurnal temperature oscillations at this depth.

A comparison of the model and observed water temperatures at one thermistor string in shown in Fig. 4. There is a distinct bias near the ocean surface where the model temperatures are too warm. For the cooler waters at depth, the scatter is considerable, with the model predictions being as much as 2°C too warm or too cool.

When dealing with only one ray path, there is a single element of **K** that is multiplied times the corresponding element of $\mathbf{z}_R$ - $\mathbf{Hx}^F$ for each model grid cell falling within the 10 km volume around the ray path. Thus, a larger value of the element of **K** for a grid cell results in a greater modification in the model-predicted water temperature in that grid cell during the PSAS assimilation process. An analysis of **K** showed that all the larger values were at water depths from 80-300 m. Thus, the assimilation of travel time anomalies will have the greatest impact on the lower levels
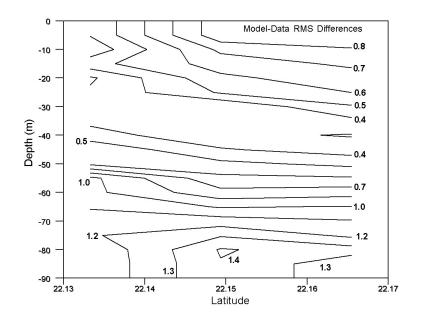

FIGURE 3. Contours (°C) of the rms differences between model-predicted water temperatures and thermistor data for July 3, 2003, without any assimilation of arrival time anomalies.
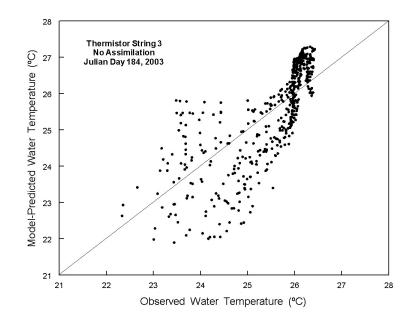
FIGURE 4. A scatter plot of observed and predicted water temperatures at one of the thermistor strings for July 3, 2003 without assimilation.

of the model grid cells, precisely where the rms differences in Fig. 3 are the largest.

During June 30-July 3, 2003, 8-11 kHz chirps (linear FM sweep) with durations of 100 ms were transmitted from D9 36 times over a 2.5-minute period every half hour. Output of each transmission was run through the matched filter process, and then the 36-transmission average was calculated. After determining the arrival times of the double surface bounce path from D9 to D12, travel time anomalies were calculated.
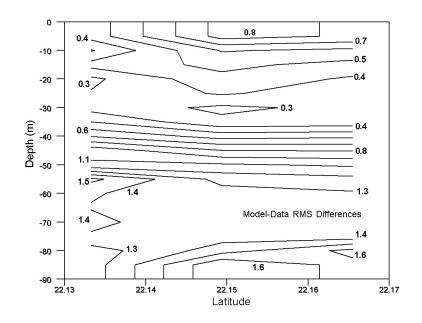

FIGURE 5. Contours (°C) of the rms differences between model-predicted water temperatures and thermistor data for July 3, 2003, with the assimilation of arrival time anomalies.
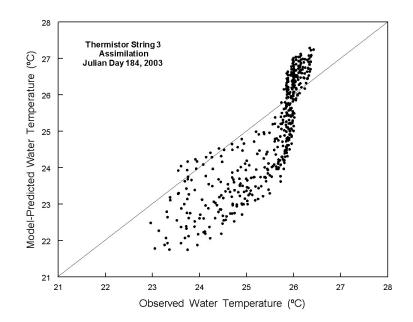
FIGURE 6. A scatter plot of observed and predicted water temperatures at one of the thermistor strings for July 3, 2003 with assimilation.

The model simulations were repeated with the assimilation of the acoustic data. The rms differences are shown in Fig. 5. We see that the rms differences have been reduced slightly in the top 30 m but increased somewhat in the lower layers of the water column.

In Fig. 6 we again show a comparison between the observed and model temperatures at the same thermistor string used in Fig. 4. We see that, although the assimilation process has reduced the scatter of the model predictions, the warmer bias near the surface still exists, and there is now a distinct cooler bias in the lower part of the water column. Comparing Figs. 4 and 6, we would conclude that assimilating the one ray path has had a positive impact on the model predictions in that it has reduced the scatter of the model water temperatures relative to the observed water temperatures. However, the assimilation has failed to eliminate the bias of the model predictions (e.g., making the surface temperatures cooler and the lower temperatures warmer in Fig. 6).

CONCLUSIONS AND RECOMMENDATIONS

We have put forward a model-oriented acoustic inversion and assimilation technique for arrival time anomalies from bottom-mounted sources and receivers. A test of this technology used arrival time anomalies from only one acoustic path. The acoustic information did not have a significant impact on reducing the rms differences between the model and observed water temperatures (Figs. 3 and 5). However, it did help in reducing the scatter of the model temperatures relative to the observed temperatures (Figs. 4 and 6).

To explain the character of the scatter plot in Fig. 6, we note that the **K** elements with the larger values were associated with water depths from 80-300 m. Thus, the

assimilation of travel time anomalies had a greater impact on the lower level model grid cells. The acoustic information resulted in a general cooling of the model temperatures (compare Figs. 4 and 6). The cooling would be applied more at the lower parts of the water column and less at the upper parts due to the values of the corresponding elements of the **K** matrix. The result is the "cold" bias in Fig. 6.

The PSAS scheme is critically dependent on the model and observation error covariance matrices. Here we approximated both error covariance matrices by $\mathbf{P_F}$. We recommend that **R** be estimated using archived model sound speed structure. Travel times could be computed using both a sophisticated acoustic propagation model and the simplified model of equation (4). Comparison of the two model results will allow us to characterize the travel time error statistics and error correlation structure.

We also need to improve the estimate of the model error covariance $\mathbf{P_F}$. If we use our most sophisticated simulations as a representation of the true ocean, we could subtract this from corresponding "degraded" model simulations. Degradations could include the exclusion of certain forcing or the use of climatological T-S fields. After subtracting the "true" ocean forecast temperatures from the degraded ocean forecast temperatures, we could then calculate the spatial covariances to obtain $\mathbf{P_F}$.

ACKNOWLEDGMENTS

REFERENCES

1. Cohn, S. E., da Silva, A., Jing Guo, Sienkiewicz, M., and Lamich, D., "Assessing the effects of data selection with the DAO Physical-space Statistical Analysis System". *Mon. Weather Rev.,* 126 (11), 1998, pp. 2913-2926.
2. Blumberg, A. F., and Mellor, G. L., "A description of a three-dimensional coastal ocean circulation model," in *Three Dimensional Coastal Models, Coastal and Estuarine Sciences, 4*, edited by N. S. Heaps, Amer. Geophys. Union Geophysical Monograph Board, 1987, pp. 1-16.
3. Smith, W. H. F., and Sandwell, D. T., "Global sea floor topography from satellite altimetry and ship depth soundings". *Science*, v. 277, 1997, pp. 1956-1962.
4. Lewis, J. K., Shulman, I., and Blumberg, A. F., "Assimilation of Doppler radar current data into ocean circulation models". *Cont. Shelf Res*., 18, 1998, pp. 541-559.
5. Egbert, G. D., "Tidal data inversion: interpolation and inference". *Prog. Oceaongr.,* 40, 1997, pp. 53-80.
6. Booij, N., Ris., R. C., and Holthuijsen, L. H., "A third-generation wave model for coastal regions, Part 1, model description and validation. *J. Geophys. Res.*, 104 (C4), 1999, pp. 7649-7666.
7. Lewis, J. K., "A three-dimensional ocean circulation model with wave effects", in *Estuarine and Coastal Modeling V*, ed. M. Spaulding and A. F. Blumberg. Am. Soc. Civil Eng., 1998, pp. 584-600.
8. Porter, M. B., and Bucker, H. P., "Gaussian beam ray tracing for computing ocean acoustic field", *J. Acoust. Soc. Am*., 82, 1987, pp. 1349-1359.-